

NJOY+NCrystal: an open-source tool for creating thermal neutron scattering libraries with mixed elastic support

Kemal Ramić^a, Jose Ignacio Marquez Damian^a, Thomas Kittelmann^a, Douglas D. Di Julio^a, Davide Campi^b, Marco Bernasconi^b, Giuseppe Gorini^b and Valentina Santoro^a

^aEuropean Spallation Source ERIC, Lund, Sweden

^bUniversity of Milano-Bicocca, Milano, Italy

ABSTRACT

In this work we present NJOY+NCrystal, a tool to generate thermal neutron scattering libraries with support for coherent and incoherent elastic components for crystalline solid materials. This tool, which is a customized version of NJOY, was created by modifying the nuclear data processing program NJOY to call the thermal scattering software library NCrystal, and includes a proposed change in the ENDF-6 format to store both the coherent and incoherent elastic components. Necessary changes to enable this format in NJOY, as well as to sample it in the OpenMC Monte Carlo code, are detailed here. Examples of materials that are coherent-dominant, incoherent-dominant, and mixed elastic scatterers are presented, as well as the creation of novel libraries for MgH₂ and MgD₂, that are under consideration as advanced neutron reflectors in the HighNESS project at the European Spallation Source. NJOY+NCrystal greatly simplifies the process to generate thermal scattering libraries (TSL) and this is exemplified with 213 new and updated TSL evaluations.

1. Introduction

The European Spallation Source, which is under construction in Lund, Sweden, will be the most powerful neutron source in the world. The source will utilize a butterfly moderator system, placed above the spallation target, to produce the brightest source of neutrons, which will be used by 15 instruments for a wide range of experiments. Recently, a project named HighNESS, [1, 2], has been initiated in order to investigate the design of a second moderator system, which would utilize a high-intensity neutron source with an emphasis on cold, very cold and ultra-cold neutrons. The project includes both the usage of novel moderator and reflector materials, in addition to enhanced techniques for producing and shaping neutron beams. Part of the effort is the creation of new accurate nuclear data describing the interaction of neutrons with these novel materials.

The design of neutron reactors, neutron sources, and nuclear systems requires calculations of neutron distributions using radiation transport codes. The source for nuclear data used in radiation transport codes, such as [3, 4, 5], are the evaluated nuclear data files (ENDF). ENDF files include sub-libraries for different kinds of particles, in particular

✉ Kemal.Ramic@ess.eu (K. Ramić); marquezj@ess.eu (J.I. Marquez Damian); Thomas.Kittelmann@ess.eu (T. Kittelmann); Douglas.DiJulio@ess.eu (D.D. Di Julio); davide.campi@epfl.ch (D. Campi); marco.bernasconi@unimib.it (M. Bernasconi); giuseppe.gorini@unimib.it (G. Gorini); Valentina.Santoro@ess.eu (V. Santoro)
ORCID(s):

thermal neutron scattering data in form of thermal scattering laws (TSL) and written in ENDF-6 format [6]. In ENDF format, File 7 stores the thermal neutron scattering data in two sections: one for elastic and one for inelastic scattering. In general, the scattering cross section of neutrons can be decomposed into four parts: coherent elastic, incoherent elastic, coherent inelastic, and incoherent inelastic scattering. Elastic scattering represents the scattering of a neutron without the exchange of energy with the target material in the laboratory frame of reference, while inelastic scattering represents the scattering of a neutron where it either gains or loses energy. Coherent scattering contains the interference terms of the scattering and therefore is sensitive to the structure of the material, whereas incoherent elastic scattering depends on the self correlation for each atom at different times.

At the moment, in the ENDF-6 format, the elastic section stores either the coherent elastic or incoherent elastic cross section only. In the inelastic section, either the incoherent inelastic cross section is stored in the incoherent approximation or the inelastic is stored as a sum of incoherent and coherent inelastic parts calculated from the coherent one-phonon approximation. To overcome the limitation in the elastic section, a change was recently proposed [7] for the thermal scattering format, which will in this paper be referred to as the “mixed elastic format”. The new format proposes to store both the coherent and incoherent elastic cross sections in the elastic section, one after another one, in the same format as in which they were stored before individually.

Thermal scattering files can be produced with the LEAPR module of NJOY [8], which is a nuclear data processing code developed by Los Alamos National Laboratory and it is an industry standard in its class of codes. As mentioned, the LEAPR module can be used for creation of TSL files, and although it has been widely used to do so, it has some limitations. Mainly, LEAPR has a limited support for coherent elastic scattering physics through few hard-coded materials (seen in Table 1), the inelastic component can be only calculated in the incoherent approximation, and it is limited by the physics that can be stored in ENDF format. On the other hand, the NCrystal library [9, 10] has an extensive treatment of the calculation of thermal neutron scattering cross sections directly but cannot generate ENDF-6 formatted files. NCrystal supports a range of physics, including coherent and incoherent elastic scattering as well as the inelastic scattering, in a wide range of materials, including powders, mosaic single crystals, layered single crystals and liquids, and it also contains a data library covering many materials important at neutron scattering facilities. In the current ENDF-6 format, most of the physics enabled in NCrystal could not be stored in the tsl-ENDF file, hence in this work we propose to combine these two tools, using NCrystal to generate the microscopic

data that is later used by NJOY to produce thermal scattering libraries for poly-crystalline (or sometimes referred to as crystals treated in the powder approximation) materials. Additionally, we include modifications to support the proposed mixed elastic format for tsI-ENDF files and produce thermal scattering .ACE files, in the here proposed format with both coherent and incoherent elastic scattering components. With NJOY+NCrystal, the user isn't anymore limited to materials with hard-coded options, but any solid poly-crystalline material can be calculated with support for coherent and incoherent elastic components in the current ENDF format, as well as in the proposed mixed elastic format. The Monte Carlo code OpenMC [4] was modified as well to support this new format of .ACE files, which makes this a complete implementation, starting from microscopic calculations and ending with Monte Carlo sampling.

2. Theory

As presented in [9], the scattering of neutrons can be represented in terms of the double differential scattering cross section as:

$$\frac{d^2\sigma_{\vec{k}\Rightarrow\vec{k}'}^-}{d\Omega'dE'} = \frac{k'}{k} S(\vec{Q}, \omega) \quad (1)$$

where σ is the cross section, $d\Omega'$ is the scattering angle, dE' is the scattered energy of neutron, k and k' are wavenumbers for the incoming and scattered neutron, $\hbar\vec{Q}$ is the momentum transfer, equal to $\hbar\vec{Q} = \hbar\vec{k}' - \hbar\vec{k}$. $S(\vec{Q}, \omega)$ is the scattering function, which for a crystalline system is divided into an equivalent subsystem and can be represented as:

$$S(\vec{Q}, \omega) = \frac{1}{2\pi\hbar} \sum_{jj'=1}^{N_{sub}} \overline{b_j b_{j'}} \int_{-\infty}^{\infty} \langle j, j' \rangle e^{-i\omega t} dt \quad (2)$$

where N_{sub} represents the subsystem size, $\overline{b_j b_{j'}}$ are the average scattering lengths over the subsystem, and $\langle j, j' \rangle$ is the expectation value at thermal equilibrium which correlates the position of the nucleus j at time t with the position of the nucleus j' at time 0 and it has form $\langle e^{-i\vec{Q}\cdot\vec{R}_{j'}(0)} e^{-i\vec{Q}\cdot\vec{R}_j(t)} \rangle$. The scattering function of such a system can then be represented as a sum of coherent and incoherent parts:

$$S(\vec{Q}, \omega) = S_{coh}(\vec{Q}, \omega) + S_{inc}(\vec{Q}, \omega) \quad (3)$$

$$S_{coh}(\vec{Q}, \omega) = \frac{1}{2\pi\hbar} \sum_{j,j'=1}^{N_{sub}} \overline{b_j} \cdot \overline{b_{j'}} \int_{-\infty}^{\infty} \langle j, j' \rangle e^{-i\omega t} dt \quad (4)$$

$$S_{inc}(\vec{Q}, \omega) = \frac{1}{2\pi\hbar} \sum_{j=1}^{N_{sub}} \left(\overline{b_j^2} - (\overline{b_j})^2 \right) \int_{-\infty}^{\infty} \langle j, j \rangle e^{-i\omega t} dt. \quad (5)$$

where $\langle j, j' \rangle$ is dependent on positions of the nuclei in a crystal. This correlation can be further simplified by applying the *harmonic approximation* which consists in separating the position operator in displacements \vec{u} from equilibrium positions \vec{d} . The resulting correlation between displacements can be expanded in a Taylor series:

$$e^{\langle (\vec{Q} \cdot \vec{u}_{j'}(0)) (\vec{Q} \cdot \vec{u}_j(t)) \rangle} = \sum_{n=0}^{\infty} \frac{1}{n!} \left(\langle (\vec{Q} \cdot \vec{u}_{j'}(0)) (\vec{Q} \cdot \vec{u}_j(t)) \rangle \right)^n \quad (6)$$

The first term in this expansion corresponds to elastic scattering. The correlation in this term is known as the Debye-Waller function:

$$W_j(\vec{Q}) \equiv \frac{1}{2} \langle (\vec{Q} \cdot \vec{u}_j(0))^2 \rangle. \quad (7)$$

For isotropic systems (i.e. polycrystalline samples), integration over all orientations results in a Q-dependent Debye-Waller function:

$$2W(Q) = \frac{1}{3} Q^2 \langle u^2 \rangle, \quad (8)$$

where $\langle u^2 \rangle$ is the mean-squared displacement (MSD).

2.1. Incoherent elastic scattering

For elastic scattering, with $k = k'$, the incoherent elastic double differential scattering cross section is equal to:

$$\begin{aligned} \frac{d^2 \sigma_{\vec{k} \rightarrow \vec{k}'}^{el,inc}}}{d\Omega' dE'} &= \frac{k'}{k} S_{el}^{inc}(\vec{Q}, \omega) \\ &= \sum_{j=1}^{N_{sub}} \left(\overline{b_j^2} - (\overline{b_j})^2 \right) e^{-2W_j(\vec{Q})} \delta(\hbar\omega). \end{aligned} \quad (9)$$

where the bound incoherent cross section, σ_b^{inc} , is equal to $\sigma_b^{inc} = 4\pi(\overline{b_j^2} - (\overline{b_j})^2)$. In NJOY, the incoherent elastic cross section is calculated in the THERMR module as:

$$\frac{d^2 \sigma_{\vec{k} \rightarrow \vec{k}'}^{el,inc}}{d\Omega' dE'} = \frac{\sigma_b^{inc}}{4\pi} e^{-2W(Q)} \quad (10)$$

with:

$$2W(Q) = 2W_{ENDF} E(1 - \mu) \quad (11)$$

where E is the incident energy of the neutron, μ is the cosine of the scattering angle, and W_{ENDF} is the Debye-Waller integral in eV^{-1} and is computed from the phonon spectrum in the LEAPR module of NJOY:

$$W_{ENDF} = \frac{\hbar^2}{2MkT} \int_0^\infty \frac{\rho(\omega)}{\hbar\omega/kT} \coth(\hbar\omega/(2kT)) d\omega \quad (12)$$

W_{ENDF} and σ_b^{inc} are stored in the incoherent elastic section of the ENDF file by LEAPR if the incoherent elastic cross section is present. The integrated incoherent elastic cross section is equal to:

$$\sigma_{el,inc}(E) = \frac{\sigma_b^{inc}}{2} \left\{ \frac{1 - e^{-4W_{ENDF}E}}{2W_{ENDF}E} \right\}. \quad (13)$$

2.2. Coherent elastic scattering

The scattering function for the coherent elastic component can be written as:

$$S_{el}^{coh}(\vec{Q}, \omega) = \frac{(2\pi)^3 \delta(\hbar\omega)}{V_{uc}} \sum_{hkl} \delta(\vec{Q} - \vec{\tau}_{hkl}) |F(\vec{\tau}_{hkl})|^2, \quad (14)$$

where V_{uc} is the volume of the unit cell, $|F(\vec{\tau}_{hkl})|$ is the form factor of the unit cell, and $\vec{\tau}_{hkl}$ is a point in the reciprocal lattice. In the powder approximation, where the crystal grains appear with uniformly randomised orientations, the integrated coherent elastic scattering cross section can be written as:

$$\sigma_{el,coh}^{hkl}(E) = \frac{\pi^2 \hbar^2}{m_n E V_{uc}} \sum_{hkl}^{E_{hkl} \leq E} d_{hkl} |F(\vec{\tau}_{hkl})|^2, \quad (15)$$

where $E_{hkl} = \frac{\hbar^2 \tau_{hkl}^2}{8m_n}$ is the energy threshold of the Bragg edge caused by the family of planes with Miller indices (hkl) , and d_{hkl} is the d-spacing of the planes. In the ENDF-6 format this information is stored as pairs $(E_{hkl}, E_{hkl} \sigma_{el,coh}^{hkl})$.

2.3. Inelastic scattering

The $n \geq 1$ terms in the expansion of eq. 6 correspond to inelastic scattering. In NJOY+NCrystal this is handled by the LEAPR module, in which the double differential scattering cross section is defined in the incoherent approximation as:

$$\frac{d^2 \sigma_{\vec{k} \rightarrow \vec{k}'}^{inelas}}{d\Omega' dE'} = \frac{\sigma_b}{4\pi kT} \sqrt{\frac{E'}{E}} S^{LEAPR}(\alpha, \beta), \quad (16)$$

where μ is the cosine of the scattering angle, and $S^{LEAPR}(\alpha, \beta)$ is the scattering function. This is different from the previous definition in eq. 1 because in the incoherent approximation the bound atom scattering cross section is factored out. The variables α and β are related respectively to the momentum transfer and energy transfer:

$$\alpha = \frac{E' + E - 2\mu \sqrt{E'E}}{Ak_B T}, \quad \beta = \frac{E' - E}{k_B T}. \quad (17)$$

where A is the ratio of the mass of the scattering atom to the neutron mass. In the incoherent and Gaussian approximation the $S(\alpha, \beta)$ is defined as:

$$S^{\text{LEAPR}}(\alpha, \beta) = \frac{1}{2\pi} \int_{-\infty}^{\infty} e^{i\beta\hat{t}} e^{-\gamma(\hat{t})} d\hat{t}, \quad (18)$$

where:

$$\gamma(\hat{t}) = \alpha \int_{-\infty}^{\infty} P(\beta)[1 - e^{-i\beta\hat{t}}] e^{-\beta/2} d\beta, \quad (19)$$

with:

$$P(\beta) = \frac{\rho(\beta)}{2\beta \sinh(\beta/2)}, \quad (20)$$

where $\rho(\beta)$ is the phonon spectrum, and \hat{t} is the time measured in units of \hbar/kT .

The total inelastic cross section is obtained by integrating eq. 16 in outgoing energy and scattering angle:

$$\sigma_{inel}(E) = \int_{4\pi} d\Omega' \int_0^{\infty} dE' \frac{d^2\sigma_{inelas}}{d\Omega' dE'} \quad (21)$$

2.4. Total cross section

The total interaction probability for an incident energy E will be given by the sum of the absorption cross section (representing the probability of all events that are not scattering), the inelastic cross section (eq. 21, and the coherent (eq. 15 and incoherent (eq. 13) elastic cross sections, if present:

$$\sigma_{tot}(E) = \sigma_{abs}(E) + \sigma_{inel}(E) + \sigma_{el,coh}(E) + \sigma_{el,inc}(E) \quad (22)$$

3. Implementation

NJOY+NCrystal was motivated mainly by a need to implement the mixed elastic format proposal in an open source code, such as NJOY. Additionally, the motivation was to provide an implementation of both a proper and user-friendly handling of the coherent and incoherent elastic cross section calculations, in both the current and proposed format, in NJOY by utilizing NCrystal. Therefore, NJOY+NCrystal is a customized version of NJOY that relies on NCrystal to provide the necessary information for the calculations of the coherent and incoherent elastic components, whereas the inelastic component will be calculated in LEAPR module of NJOY+NCrystal. Additionally, both NJOY and NCrystal utilize CMake and GitHub Repository's for the installation, hence making the integration smoother.

The changes to NJOY can be split into two parts. The first part is to provide an interface between LEAPR and NCrystal, described briefly in 3.1, so that LEAPR can calculate coherent and incoherent elastic cross section components for any crystalline material. The calculated elastic components are then stored in the tsl-ENDF file for both the current and proposed mixed elastic format. The second part consists of implementing changes to the THERMR and ACER modules of NJOY so that the new mixed elastic format can be read and handled properly in order to produce .ACE files used by Monte Carlo programs to sample neutron scattering events. The changes to the OpenMC Monte Carlo transport code are presented in Section 3.3, as an example of the sampling here proposed mixed elastic .ACE format.

3.1. LEAPR modifications

In the current LEAPR module of NJOY, which is used to prepare the scattering law in ENDF-6 format, there are a few hard coded options for the coherent elastic component, given by the `ie1` flag in the input deck: `ie1 = 0` for no coherent elastic contribution, and options `ie1 = 1-6` for hard coded materials (Table 1). For the implementation of the mixed-elastic proposal, a new option (`ie1 = 100`, hereinafter referred to as MEF option) was added, which calculates and stores the parameters for the coherent and incoherent elastic components, as described in the proposed format. Since this change has not yet been widely adopted, an additional (`ie1 = 99`) option is provided to control the output of elastic data in the tsl-ENDF file using the current ENDF format (CEF), and hereinafter `ie1 = 99` option will be referred to as CEF option.

Table 1
Elastic options in LEAPR.

ie1	Description
0	No coherent calculation.
1	Graphite (hard coded in LEAPR).
2	Beryllium (hard coded in LEAPR).
3	Beryllium oxide (hard coded in LEAPR).
4	Aluminum (hard coded in LEAPR).
5	Lead (hard coded in LEAPR).
6	Iron (hard coded in LEAPR).
...	Reserved.
99	Compute TSL in the current ENDF format (CEF).
100	Compute TSL in the proposed mixed elastic format (MEF).

3.1.1. Mixed elastic format, MEF

Coherent scattering is a property of the system (Equation 4), whereas incoherent scattering can be assigned individually to atoms (Equation 5). In the ENDF-6 format, the scattering has to be decomposed into the contribution from the different elements. With this in mind, in the MEF option, the thermal scattering library for each element that composes a material contains two parts: coherent scattering divided by the total number of atoms in the system, and the incoherent scattering that corresponds to the atom (as can be seen in Figure 1):

$$\sigma_i^{\text{el}}(E, \mu) = \sigma^{\text{coh}}(E, \mu)/N + \sigma_i^{\text{inc}}(E, \mu). \quad (23)$$

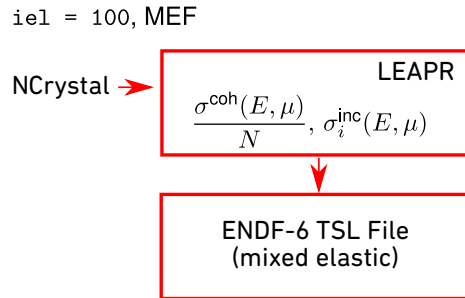


Figure 1: Simplified flow of NJOY+NCrystal when the MEF option is used.

3.1.2. Current ENDF format, CEF

In the CEF option, only the coherent or incoherent scattering model can be used, but not both. For systems with only one type of atom (e.g. Al, Fe, Si), the major component is stored but it is scaled to the total bound scattering cross section (as can be seen in Figure 2) to ensure the proper asymptotic behavior in the epithermal range:

$$\sigma_i^{\text{el}}(E, \mu) = \frac{\sigma_b^{\text{coh}} + \sigma_b^{\text{inc}}}{\sigma_b^{\text{coh}}} \sigma^{\text{coh}}(E, \mu), \quad \text{if } \sigma_b^{\text{coh}} > \sigma_b^{\text{inc}}, \quad (\text{coherent approximation}) \quad (24)$$

$$\sigma_i^{\text{el}}(E, \mu) = \frac{\sigma_b^{\text{coh}} + \sigma_b^{\text{inc}}}{\sigma_b^{\text{inc}}} \sigma_i^{\text{inc}}(E, \mu), \quad \text{if } \sigma_b^{\text{coh}} \leq \sigma_b^{\text{inc}}, \quad (\text{incoherent approximation}) \quad (25)$$

ie1 = 99, CEF (single atom case)

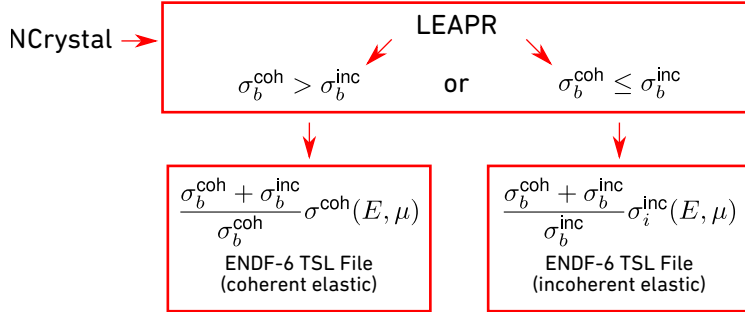


Figure 2: Simplified flow of NJOY+NCrystal when the CEF option is used for a monatomic scatterer.

For systems with more than one atom, the contributions are sorted and the atom with the minimum incoherent contribution (called *designated coherent*, DC) is stored in the coherent approximation. Its incoherent contribution, if it exists, is distributed among the rest of the elements which are stored in the incoherent approximation (as can be seen in Figure 3):

$$\sigma_{\text{mol}}^{\text{el}}(E, \mu) = N \left[\sigma^{\text{coh}}(E, \mu) / N \right] + N_{\text{DC}} \sigma_{\text{inc}}^{\text{DC}}(E, \mu) + \sum_{i \neq \text{DC}} N_i \sigma_{\text{inc}}^i(E, \mu)$$

$$\begin{aligned}
 &= N_{\text{DC}} \left[\sigma^{\text{coh}}(E, \mu) / (N f_{\text{DC}}) \right] + \sum_{i \neq \text{DC}} N_i \left[\sigma_{\text{inc}}^i(E, \mu) + \frac{f_{\text{DC}}}{1 - f_{\text{DC}}} \sigma_{\text{inc}}^{\text{DC}}(E, \mu) \right] \\
 &\approx N_{\text{DC}} \left[\sigma^{\text{coh}}(E, \mu) / (N f_{\text{DC}}) \right] + \sum_{i \neq \text{DC}} N_i \left[1 + \frac{f_{\text{DC}}}{1 - f_{\text{DC}}} \frac{\sigma_{b,\text{DC}}^{\text{inc}}}{\sigma_{b,i}^{\text{inc}}} \right] \sigma_{\text{inc}}^i(E, \mu) \quad (26)
 \end{aligned}$$

The first term in this equation is stored in the elastic component of the DC atom in the coherent approximation, and each term of the sum in the second term is stored in the rest of the atoms in the incoherent approximation. Since incoherent scattering of the designated coherent element is being redistributed between the other atoms in the molecule/compound, the approximation made in the last step implies using the Debye-Waller factor of the rest of the components to account for the missing incoherent scattering of the designated coherent element.

i.e1 = 99, CEF (molecule or compound)

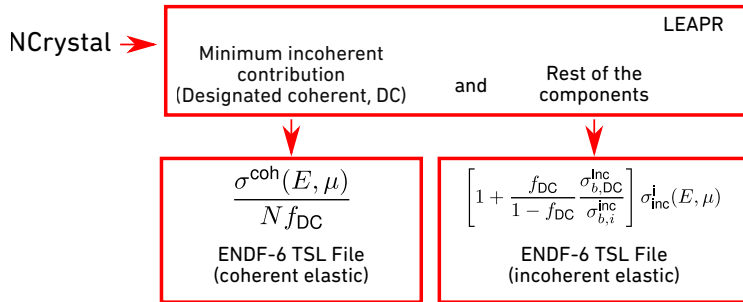


Figure 3: Simplified flow of NJOY+NCrystal when the CEF option is used for a polyatomic or molecular scatterer.

If the mixed-elastic proposal cannot be used, the calculation of the CEF option using NJOY+NCrystal provides a reasonable approximation within the limitations of the format. It is important to note that the CEF option is currently supported in standard versions of MCNP and PHITS, whereas the MEF option requires modifications. Examples of this are provided in Section 4. It is also important to note that both the CEF and the MEF options will only provide the right answer if they are used in the correct stoichiometry.

3.1.3. Wrapper function

For the CEF and MEF options, LEAPR calls a wrapper function (since NJOY2016 is written in Fortran while NCrystal is in C++ programming language) that for the coherent elastic component obtains a list of Bragg edges, given as pairs of energy and cross section data for each Bragg edge from NCrystal. The wrapper function also passes to LEAPR the values for the bound coherent and incoherent elastic cross sections, as well as the free atom cross section for the nuclide that is being processed in LEAPR, which is used for consistency between the inelastic and elastic components. These cross sections are obtained from a builtin library inside NCrystal, which includes data for all the major elements and isotopes. Since the elastic component is handled by NCrystal and the inelastic by LEAPR module of NJOY+NCrystal, an additional consistency check is performed by comparing the mean squared displacement (MSD) values from the two codes for the nuclide that is being processed in LEAPR. The wrapper function passes to LEAPR the NCrystal MSD value and both NCrystal and NJOY+NCrystal values for MSD are stored in the output file of the LEAPR module. Since both the inelastic and elastic component exhibit dependence on the phonon spectrum (for the elastic component the dependence is through Debye-Waller integral as seen in Equations 8,11,12, and for the inelastic dependence can be seen in Equations 18,19,20), the check of the MSD values is also a check on whether the same phonon spectrum is used in both the NCrystal and NJOY+NCrystal input files. The LEAPR value of MSD can be calculated from W_{ENDF} , as defined in Equation 12, as follows:

$$\langle u^2 \rangle = \frac{\hbar^2 W_{\text{ENDF}}}{2m_n}, \quad (27)$$

where m_n is the mass of neutron in units of $\text{eV} \cdot \text{ps}^2 \cdot \text{\AA}^{-2}$, and \hbar^2 is Planck's constant in units of $\text{eV} \cdot \text{ps}$.

3.2. THERMR/ACER modifications

The modules THERMR and ACER of NJOY were also modified to implement processing of the tsl-ENDF proposed mixed elastic format, as well as to produce .ACE files in a format that is being proposed here, since at the time of the development of the code no official format for mixed elastic implementation in .ACE files has been developed or announced. THERMR reconstructs the double differential cross section and produces pointwise ENDF files (PENDF tapes) from tsl-ENDF files, and ACER processes PENDF files into .ACE files.

THERMR reads the tsl-ENDF file and handles the elastic section according to the `lthr` flag: `lthr=1` for coherent

Header							
Name	AWR	Temperature	Date				
Title							
IZAW array (ZAID assignments)							
ZAID ₁	0.	ZAID ₂	0.	...			
NXS Array							
Length of second block of data	IDPNI Inelastic scattering mode	NIL Inelastic dimensioning parameter	NIEB Number of inelastic exiting energies	IDPNC Elastic scattering mode	NCL Elastic dimensioning parameter	IFENG Secondary energy mode	NCL2 Second elastic dimensioning parameter
JXS Array							
ITCE Inelastic energy table	ITIX Inelastic cross sections	ITXE Inelastic energy/angle distributions	ITCE Elastic energy table	ITCX Elastic cross sections	ITCA Elastic angular distributions	ITCE2 Second elastic energy table	ITCX2 Second elastic cross sections
	ITCA2 Second elastic angular distributions						
XSS Array							

Figure 4: Proposed format for the thermal .ACE files with mixed elastic. Changes are highlighted in red.

elastic, `1thr=2` for incoherent elastic or here proposed `1thr=3` for mixed elastic. There are no changes to the THERMR input deck and the `1thr` flag is set during the writing process of the `tsl-ENDF` file in LEAPR.

In the ACER input deck, an additional option for the `ielas` flag was added. Option `ielas=0` processes the PENDF tape as coherent elastic, `ielas=1` processes the file as incoherent elastic, and the here proposed `ielas=2` as mixed elastic. The .ACE format [11] requires changes to store the additional data for the mixed elastic contributions, and the changes we propose in this work can be seen in Figure 4. In the proposed format, the flag `IDPNC=5` is reserved for mixed elastic, and four additional integers are stored in the NXS and JXS control arrays. `NCL2` determines the dimension of the second elastic block, `ITCE2` gives the position of the energy table for the second elastic block, `ITCX2` gives the position of the cross section table for the second elastic block, and `ITCA2` gives the position of the angular distribution. In this implementation of the mixed elastic format of .ACE files, the first elastic block is coherent and the second elastic block is an incoherent elastic component.

3.3. OpenMC modifications

As a proof of concept implementation we modified OpenMC to read and use .ACE files in the proposed mixed elastic format. The Python API was modified to read mixed elastic .ACE files and as well to read and write HDF5 files in mixed elastic format. The C++ calculation engine was modified to add the second elastic component to the total cross section if it is present and to sample both elastic reactions. The modifications to OpenMC can be found at [12].

4. Example evaluations

Using NJOY+NCrystal, 213 tsl-ENDF evaluations were created for 112 new or updated materials. A summary of the NJOY+NCrystal library is given in Tables 3-7. In this section, a few materials will be highlighted, which include tin as an example of a coherent scatterer, vanadium as an incoherent scatterer, nickel as mixed elastic scatterer, and MgH_2 and MgD_2 are shown as relevant materials to the HighNESS project.

For the materials in Tables 3-7, different methodologies were employed to create the final tsl-ENDF files. Some of the materials were created from existing .NCMAT files in current and previous versions of NCrystal. For some of the materials, mostly monoatomic metals, VDOS curves in existing .NCMAT files were updated, mostly using different sources from the literature. For MgH_2 and MgD_2 , detailed DFT calculations were performed and the details can be found in Section 4.4. For the rest of the materials, phonon curves were obtained by utilizing ab-initio calculations from a phonon database at Kyoto University [13, 14, 15, 16]. In summary, the files from the database were used with Phonopy [17] to calculate phonon eigenvalues and eigenfrequencies, which were then utilized with oClimax [18] to extract partial phonon spectra. A detailed explanation of how the phonon spectrum and crystal structure was obtained for each material is provided in the comments section of the tsl-ENDF files.

The experimental data for the validation of the tsl-ENDF files is scarce. Wherever the experimental data were available, tsl-ENDF files were validated against total cross section measurements and diffraction data, while all materials were validated against specific heat capacity curves as a minimum standard for acceptance. The last column of Tables 3-7 contains information on the valid temperature range for each material, references for VDOS curves, and a list of validations applied. For the VDOS curves a reference is provided, where for the ones calculated with Phonopy and oClimax the reference to Kyoto University phonon database is given. The link to the exact files used for each material at Kyoto University database can be found inside the tsl-ENDF files in the Highness Github repository. For validation, the correct crystal structure was a starting point (a reference for each crystal structure can be found inside tsl-ENDF files as well), followed by comparison with the experimental specific heat capacity and if available, total cross section measurements. For α and β SiC, diffraction data was used as well as a means of validation of the libraries.

4.1. Tin

With $\sigma_{\text{inc}} = 0.022$ b and $\sigma_{\text{coh}} = 4.870$ b, tin is a mainly coherent scatterer. Using NJOY+ NCrystal we have created tsl-ENDF and .ACE files for tin, and compared the calculated total cross section with measurements by Mayer[19, 20], retrieved from EXFOR[21] (Figure 5). In this comparison, both scattering and absorption are included, using $\sigma_{2200} = 0.626$ b. For completeness, the total cross section from the .ACE files, prepared by NJOY+ NCrystal, was plotted using OpenMC and the results for CEF and MEF options are shown, as well as each scattering component from the MEF option.

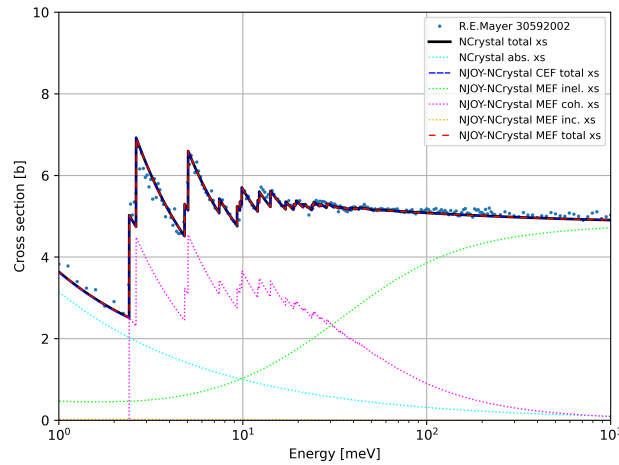


Figure 5: Total scattering cross section comparison for tin.

In Figure 5 it can be observed that the agreement between the experimental total cross sections and the calculated cross sections for NCrystal, and using both CEF and MEF options in NJOY+NCrystal is very good (all three lines are overlaid on top of each other). Therefore, for predominantly coherent materials like tin, the CEF option performs nearly as well as the MEF option, and it can be used even without the mixed-elastic format.

4.2. Vanadium

Vanadium is a common example of a mostly incoherent material, with $\sigma_{\text{inc}} = 5.08$ b and $\sigma_{\text{coh}} = 0.018$ b. The calculated cross sections were obtained in the same manner as for tin.

As can be seen from Figure 6, the calculated total cross sections, including $\sigma_{2200} = 5.08$ b, are in excellent agreement with the experimental total cross section measurements from Vertebynj [22] and Palevsky [23]. The coherent elastic component is negligible, while the incoherent elastic component is dominant. Again, the CEF option provides

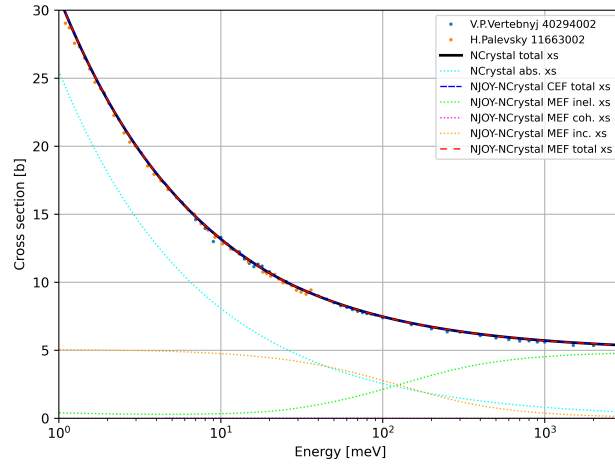


Figure 6: Total scattering cross section comparison for vanadium.

an adequate representation of the total cross section for Vanadium.

4.3. Nickel

Nickel, with $\sigma_{inc} = 5.2$ b and $\sigma_{coh} = 13.3$ b, has a significant contribution from both coherent and incoherent scattering. This, in the current ENDF-6 format, can only be approximated correctly to a certain degree.

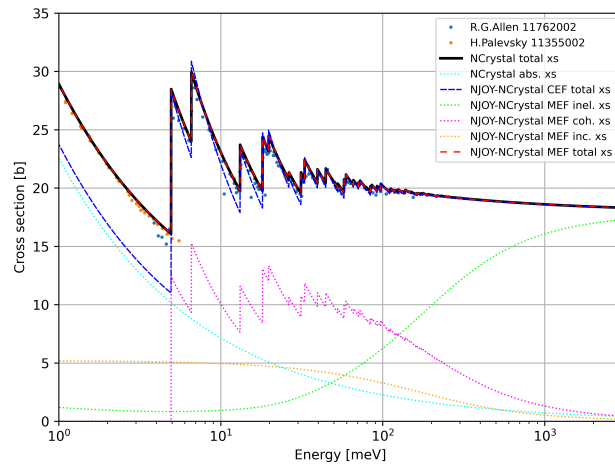


Figure 7: Total scattering cross section comparison for nickel.

In Figure 7 we compare the calculated total cross sections, including $\sigma_{2200} = 4.49$ b, with experimental data from Allen [24, 25] and Palevsky [26, 27]. In this plot it can be seen that the agreement of the NCrystal and the total cross section curve calculated with the MEF option with the experimental data is excellent, while the agreement for the CEF option curve is good in the region above the first Bragg edge. Since the CEF option scales the major elastic component,

in this case the coherent elastic part (Equation 24), by the total bound incoherent plus coherent scattering cross section, the total cross section below the first Bragg edge only contains the contribution from the inelastic component and hence differs significantly. There is also some discrepancy above the first Bragg edge as well for CEF option, which is due to the fact that coherent elastic scaling provides the correct epithermal asymptotic behavior but only approximates the low energy region. Thus this demonstrates the importance for the ENDF-6 format to support the capability to store both the coherent and incoherent elastic scattering components.

As mentioned in Section 3.3, changes to OpenMC were implemented so that the new format can be used to sample thermal scattering events. Figure 8 shows the results of a simple transmission Monte Carlo calculation, which includes a mono-energetic neutron beam on a 5 mm thick slab of nickel. The total cross section curve was obtained from the ratio of the incident and the transmitted neutron spectrum and we can see that the agreement between the calculation and the experimental data, as well as the total cross section calculated in the MEF option, is excellent. The discrepancy at the lower energies is caused by differences in the absorption cross section in ENDF/B-VIII.0 library ($\sigma_{2200} = 4.09$ b) and NCrystal ($\sigma_{2200} = 4.49$ b).

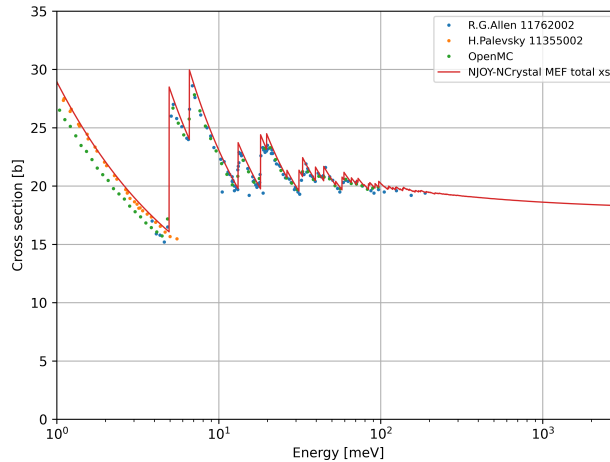


Figure 8: OpenMC calculation of the simplified transmission experiment on nickel. The difference in the low energy region is caused by differences in the absorption cross section. NCrystal uses $\sigma_{2200} = 4.49$ barns whereas in ENDF/B-VIII.0 $\sigma_{2200} = 4.09$ barns.

4.4. $\text{MgD}_2/\text{MgH}_2$

As an additional example of the capabilities of NJOY+ NCrystal, related to the HighNESS project, we computed the total scattering neutron cross sections of polycrystalline MgH_2 and its deuterated variant MgD_2 . MgH_2 recently

emerged as a good candidate material for cold neutron reflectors [28], while MgD_2 , because of an even lower absorption cross section, is also investigated here.

Phonon spectrum calculations were performed using Density Functional Perturbation Theory (DFPT) [29] with the Perdew-Burke-Ernzerhof (PBE) [30] approximation to the exchange and correlation energy functional. Ultrasoft pseudopotentials [31, 32] and a plane wave expansion of Kohn-Sham orbitals up to a kinetic cutoff of 60 Ry was employed, as implemented in the Quantum-ESPRESSO package [33]. In the electronic structure calculations, the Brillouin zone (BZ) integration was performed over a uniform Γ -centered $10 \times 10 \times 14$ \mathbf{k} -point mesh [34].

MgH_2 crystallizes in the rutile structure ($P4_2/mmm$ space group) with six atoms per unit cell [35]. Geometry optimization yields the theoretical equilibrium lattice parameters $a=4.512 \text{ \AA}$ and $c=3.010 \text{ \AA}$ which are very close to the experimental values of $a=4.5025 \text{ \AA}$ and $c=3.0123 \text{ \AA}$ as measured from X-ray scattering [35]. The dynamical matrix is computed within DFPT on a $4 \times 4 \times 6$ \mathbf{q} -mesh. Short range force constants were then obtained by Fourier transforming the dynamical matrices over the \mathbf{q} -mesh after subtracting the contribution from point charges as described in [29]. The force constants then allow computing the phonon spectrum on a fine \mathbf{q} -mesh [29].

The phonon dispersion relations and the DOS of MgH_2 and MgD_2 are compared in Figures 9-10. The results for MgH_2 are very similar to previous ab-initio works [36, 37]. In particular, in [36] the overall validity of the isotropic approximation of the mean square displacement is assessed at different temperatures. The high-frequency phonons, due to the motion of hydrogen, are almost exactly scaled by a factor $\sqrt{2}$ by isotopic substitution while the acoustic part of the spectrum is essentially unchanged.

The neutron-weighted phonon density of states, computed by multiplying the projected DOS with the corresponding total neutron scattering cross section [38], is compared in Figure 11 with the experimental spectrum from inelastic neutron scattering data [39]. The agreement between theory and experiment is overall good, although a sizable error is present in the position of the peak at about 600 cm^{-1} . A good agreement between theory and experiments is also found for the frequency of the Raman active modes (Γ point) as shown in Table 2.

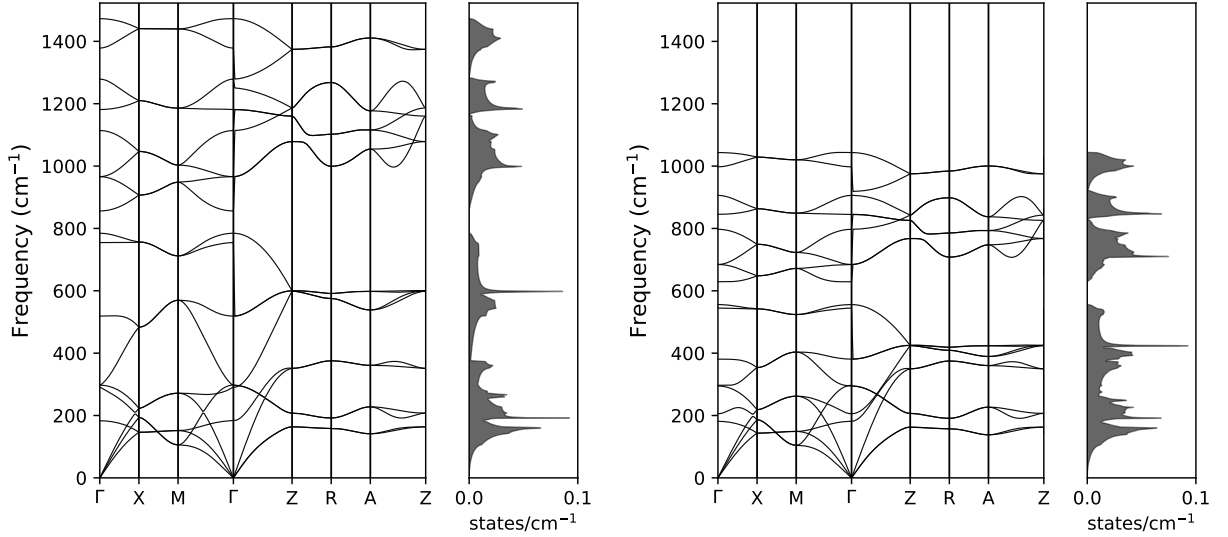


Figure 9: Theoretical phonon dispersion relations along high-symmetry directions in the Brillouin zone and total phonon density of states for (left) MgH_2 and (right) MgD_2 .

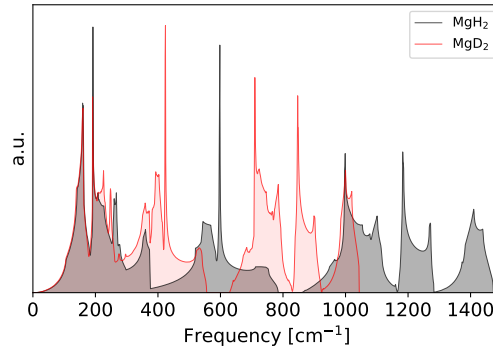


Figure 10: Comparison of the theoretical phonon DOS for MgH_2 and MgD_2 . The density of states have been computed using the tetrahedron method using a $20 \times 20 \times 30$ \mathbf{q} -grid for interpolation.

Table 2

Theoretical (this work) and experimental [40] frequency (cm^{-1}) of Raman active modes of MgH_2 .

	Exp.	Theory
B_{1g}	302.65	290
E_g	967.36	966
A_{1g}	1295.79	1279

From the calculated phonon spectra, tsl-ENDF files were created for both MgH_2 and MgD_2 , using the NJOY + NCrystal tool. In Figure 12 it can be seen that the agreement between the measured total cross section data from Granada [28] and the calculated curves (which include an absorption cross section ($\sigma_{2200}^{\text{H}} = 0.3326$ b, $\sigma_{2200}^{\text{Mg}} = 0.063$ b) is excellent. Since MgH_2 is an incoherent scatterer, due to the large incoherent cross section of hydrogen, ie1=99 is a good option

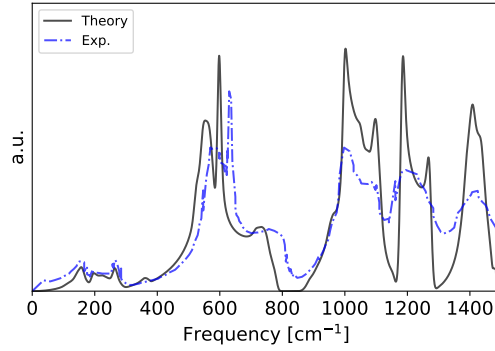


Figure 11: Neutron-weighted theoretical phonon DOS compared with an experimental spectrum from inelastic neutron scattering [39]. The theoretical density of states has been computed using the tetrahedron method using a $20 \times 20 \times 30$ \mathbf{q} -grid for interpolation and then convoluted with a Gaussian function with standard deviation of 5 cm^{-1} to better match the experimental resolution.

as well.

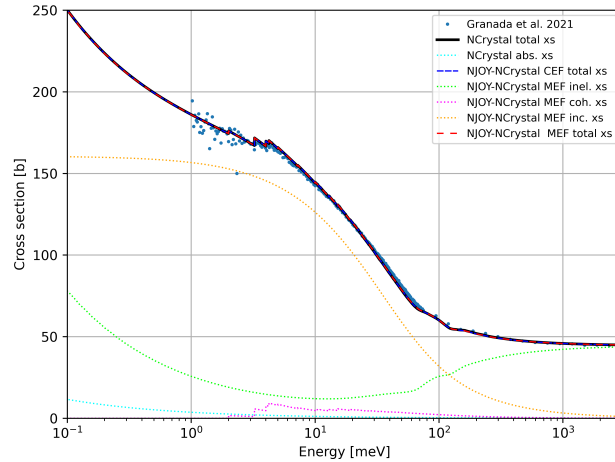


Figure 12: Total scattering cross section comparison for MgH_2 .

Figure 13 shows a comparison between the NCrystal and the NJOY+NCrystal calculated total cross sections for MgD_2 , as well as different scattering components as calculated in NJOY+NCrystal and NCrystal. The total cross section for MgD_2 is orders of magnitude lower than for MgH_2 . This is due to incoherent hydrogen, with a cross section of 82.02 barns, being replaced with coherent deuterium with the cross section of 7.64 barns. From Figure 13 we can see that both the coherent and incoherent elastic components are not negligible in the thermal region and that the agreement between NCrystal, CEF and MEF calculated total cross sections is excellent.

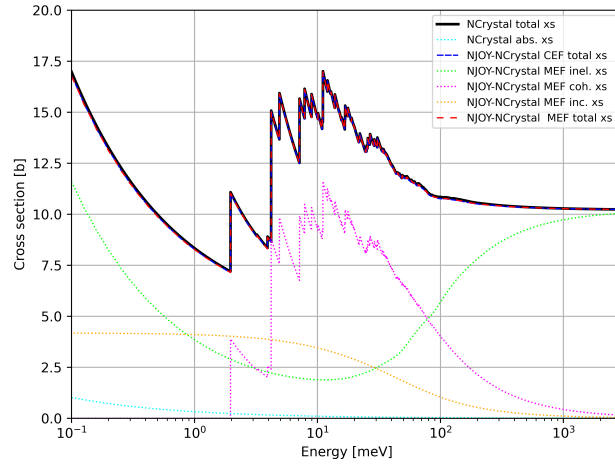


Figure 13: Total scattering cross section comparison for MgD_2 .

5. Conclusions

In this work we presented a new tool for creating thermal neutron scattering libraries for crystalline solid materials that combines the strengths of the industry standard NJOY2016 with the new capabilities of the software library NCrystal. This new tool includes the implementation of the new mixed elastic format for ENDF-6 files, as well as a proposal for mixed elastic support in the .ACE format. The tool was used to create the largest collection of thermal scattering libraries to date. Explanations of changes made to NJOY2016, to create the tsl-ENDF and .ACE files, are presented as well as the changes to OpenMC to handle .ACE files in the new format. Examples for different types of scatterers have been provided (i.e. coherent-dominant, incoherent-dominant, as well as mixed elastic scatterers) coupled with experimental data validation. Phonon spectra have also been calculated and new tsl-ENDF files, for reflector materials being considered in the HighNESS project at the ESS, have been generated.

Although NJOY+NCrystal represents significant improvement upon currently available methods for treatment of thermal neutron scattering in Monte Carlo particle codes, it is still limited by what can be stored in the ENDF-6 format. For a complete utilization of the capabilities of NCrystal, such as modelling single crystals, small angle neutron scattering, coherent one-phonon approximation, multi-phase and defects support, direct calls to NCrystal by Monte Carlo codes would need to be made. This will be the focus of future work.

All the source code presented in this work, as well as the thermal scattering libraries in tsl-ENDF and .ACE format are available in the Github repository of the HighNESS project: <https://github.com/highness-eu>.

6. Supplemental information

Supplemental information is available in the online version of this article, including plots of the total cross and heat capacity for all materials, and a text file containing the comments for each model. Numbers in the cross section plots are EXFOR entries. Experimental cross section data in the plots has not been renormalized.

7. Acknowledgements

This work was funded by the HighNESS project at the European Spallation Source. HighNESS is funded by the European Framework for Research and Innovation Horizon 2020, under grant agreement 951782.

Table 3

List of tsI-ENDF evaluations in the NJOY+NCrystal library.

Material	Name	Material Number	Components	Temperature range, VDOS reference, Validation
AgBr	Silver Bromide	1	Br(AgBr), Ag(AgBr)	20 - 700 K, [13], CS, SHC
Ag	Silver	2	Ag	20 - 1200 K, [41], CS, SHC, XS
Al2O3	Corundum	3	O(Al2O3), Al(Al2O3)	20 - 2200 K, [42], CS, SHC, XS
Al4C3	Aluminium Carbide	4	C(Al4C3), Al(Al4C3)	20 - 2400 K, [13], CS, SHC
AlN	Aluminum Nitride	5	N(AlN), Al(AlN)	20 - 2700 K, [13], CS, SHC
Al	Aluminum	6	Al	20 - 900 K, [43], CS, SHC, XS
Au	Gold	7	Au	20 - 1200 K, [44], CS, SHC, XS
BaF2	Barium Fluoride	8	F(BaF2), Ba(BaF2)	20 - 1600 K, [13], CS, SHC
BaO	Barium Oxide	9	O(BaO), Ba(BaO)	20 - 2000 K, [13], CS, SHC
Ba	Barium	10	Ba	20 - 1000 K, [45], CS, SHC, XS
Be3N2	Beryllium Nitride	12	Be(Be3N2), N(Be3N2)	20 - 2400 K, [13], CS, SHC
Bi2O3-β	Bismuth Trioxide	18	O(Bi2O3-β), Bi(Bi2O3-β)	600 - 900 K, [13], CS, SHC
Bi	Bismuth	22	Bi	20 - 500 K, [46], CS, SHC, XS
C-diamond	Diamond	23	C(C-diamond)	20 - 4000 K, [47], CS, SHC
CF4-α	Carbon Tetrafluoride	25	C(CF4-α), F(CF4-α)	20 - 70 K, [13], CS, SHC
CaCO3	Aragonite	26	C(CaCO3), O(CaCO3), Ca(CaCO3)	20 - 1000 K, [13], CS, SHC
CaF2	Calcium Fluoride	27	F(CaF2), Ca(CaF2)	20 - 1600 K, [13], CS, SHC
CaH2	Calcium Hydride	28	H(CaH2), Ca(CaH2)	20 - 1200 K, [13], CS, SHC
CaOH2	Calcium Hydroxide	29	H(CaOH2), O(CaOH2), Ca(CaOH2)	20 - 800 K, [13], CS, SHC
CaO	Calcium Oxide	30	O(CaO), Ca(CaO)	20 - 2500 K, [13], CS, SHC
CaZrO3	Calcium Zirconate	31	O(CaZrO3), Ca(CaZrO3), Zr(CaZrO3)	20 - 2500 K, [13], CS, SHC
Ca	Calcium	32	Ca	20 - 700 K, [48], CS, SHC, XS
CeO2	Cerium Oxide	33	O(CeO2), Ce(CeO2)	20 - 2500 K, [13], CS, SHC
Cr	Chromium	34	Cr	20 - 2000 K, [49], CS, SHC, XS
Cu2O	Cuprite	35	O(Cu2O), Cu(Cu2O)	20 - 1400 K, [13], CS, SHC
Cu	Copper	36	Cu	20 - 1200 K, [50], CS, SHC, XS
Dy2O3	Dysprosium Oxide	37	O(Dy2O3), Dy(Dy2O3)	20 - 2400 K, [13], CS, SHC

* CS = Crystal structure

* SHC = Specific heat capacity

* XS = Total cross section measurement

Table 4
List of tsl-ENDF evaluations in the NJOY+NCrystal library (continued)

Material	Name	Material Number	Components	Temperature range, VDOS reference, Validation
Fe- α	Alpha Iron	38	Fe(Fe- α)	20 - 1100 K, [51], CS, SHC, XS
Fe- γ	Gamma Iron	39	Fe(Fe- γ)	1200 - 1800 K, [52], CS, SHC
Ge3Bi4O12	Bismuth Germanate	43	O(Ge3Bi4O12), Ge(Ge3Bi4O12), Bi(Ge3Bi4O12)	20 - 1300 K, [13], CS, SHC
GeTe	Germanium Telluride	44	Ge(GeTe), Te(GeTe)	20 - 600 K, [13], CS, SHC
Ge	Germanium	45	Ge	20 - 1200 K, [53], CS, SHC, XS
Ho2O3	Holmium Oxide	47	O(Ho2O3), Ho(Ho2O3)	20 - 2400 K, [13], CS, SHC
KBr	Potassium Bromide	48	K(KBr), Br(KBr)	20 - 1000 K, [13], CS, SHC
KF	Potassium Flouride	49	F(KF), K(KF)	20 - 1100 K, [13], CS, SHC
KOH	Potassium Hydroxide	50	H(KOH), O(KOH), K(KOH)	20 - 500 K, [13], CS, SHC
K	Potassium	51	K	20 - 300 K, [54], CS, SHC, XS
La2O3	Lanthanum Oxide	52	O(La2O3), La(La2O3)	20 - 2500 K, [13], CS, SHC
LaBr3	Lanthanum Bromide	53	Br(LaBr3), La(LaBr3)	20 - 1000 K, [13], CS, SHC
Li2O	Lithium Oxide	54	Li(Li2O), O(Li2O)	20 - 1700 K, [13], CS, SHC
Li3N	Lithium Nitride	55	Li(Li3N), N(Li3N)	20 - 1000 K, [13], CS, SHC
LiF	Lithium Flouride	56	Li(LiF), F(LiF)	20 - 1100 K, [13], CS, SHC
LiH	Lithium Hydride	57	H(LiH), Li(LiH)	20 - 900 K, [13], CS, SHC
Lu2O3	Lutetium Oxide	58	O(Lu2O3), Lu(Lu2O3)	20 - 2400 K, [13], CS, SHC
Mg2SiO4	Magnesium Silicate	59	O(Mg2SiO4), Mg(Mg2SiO4), Si(Mg2SiO4)	20 - 2100 K, [13], CS, SHC
MgAl2O4	Magnesium Aluminate Spinel	60	O(MgAl2O4), Mg(MgAl2O4), Al(MgAl2O4)	20 - 2400 K, [13], CS, SHC
MgCO3	Magnesium Carbonate	61	C(MgCO3), O(MgCO3), Mg(MgCO3)	20 - 600 K, [13], CS, SHC
MgD2	Magnesium Deuteride	62	D(MgD2), Mg(MgD2)	20 - 600 K, CS, SHC, XS
MgH2	Magnesium Hydride	64	H(MgH2), Mg(MgH2)	20 - 600 K
MgOH2	Magnesium Hydroxide	65	H(MgOH2), O(MgOH2), Mg(MgOH2)	20 - 600 K, [13], CS, SHC
Mg	Magnesium	67	Mg	20 - 900 K, [55], CS, SHC, XS

* CS = Crystal structure

* SHC = Specific heat capacity

* XS = Total cross section measurement

Table 5
List of tsl-ENDF evaluations in the NJOY+NCrystal library (continued)

Material	Name	Material Number	Components	Temperature range, VDOS reference, Validation
Mo	Molybdenum	68	Mo	20 - 2500 K, [56], CS, SHC, XS
Na ₄ Si ₃ Al ₃ O ₁₂ Cl	Sodalite	69	O(Sodalite), Na(Sodalite), Al(Sodalite), Si(Sodalite), Cl(Sodalite)	20 - 1300 K, [13], CS, SHC
NaBr	Sodium Bromide	72	Na(NaBr), Br(NaBr)	20 - 2100 K, [13], CS, SHC
NaCl	Sodium Chloride	73	Na(NaCl), Cl(NaCl)	20 - 1000 K, [13], CS, SHC
NaF	Sodium Flouride	74	F(NaF), Na(NaF)	20 - 1200, [13], CS, SHC K
NaI	Sodium Iodide	75	Na(NaI), I(NaI)	20 - 900 K, [13], CS, SHC
NaMgH3	Sodium Magnesium Hydride	76	H(NaMgH3), Na(NaMgH3), Mg(NaMgH3)	20 - 600 K, [13], CS, SHC
NaOH	Sodium Hydroxide	77	H(NaOH), O(NaOH), Na(NaOH)	20 - 590 K, [13], CS, SHC
Na	Sodium	78	Na	20 - 350 K, [57], CS, SHC, XS
Nb	Niobium	79	Nb	20 - 2500 K, [58], CS, SHC, XS
Nd2O3	Neodymium Oxide	80	O(Nd2O3), Nd(Nd2O3)	20 - 2400 K, [13], CS, SHC
Ni	Nickel	81	Ni	20 - 1500 K, [59], CS, SHC, XS
P2O5	Phosphorus Pentoxide	82	O(P2O5), P(P2O5)	20 - 600 K, [13], CS, SHC
Pb3O4	Lead Oxide	83	O(Pb3O4), Pb(Pb3O4)	20 - 800 K, [13], CS, SHC
PbCO3	Lead Carbonate	84	C(PbCO3), O(PbCO3), Pb(PbCO3)	20 - 580 K, [13], CS, SHC
PbF2	Lead Flouride	85	F(PbF2), Pb(PbF2)	20 - 1000 K, [13], CS, SHC
PbO- α	Alpha Lead Monoxide	87	O(PbO- α), Pb(PbO- α)	20 - 1100 K, [13], CS, SHC
PbO- β	Beta Lead Monoxide	88	O(PbO- β), Pb(PbO- β)	20 - 1100 K, [13], CS, SHC
PbS	Lead Sulfide	89	S(PbS), Pb(PbS)	20 - 1300 K, [13], CS, SHC
Pb	Lead	90	Pb	20 - 600 K, [60], CS, SHC, XS
Pd	Palladium	91	Pd	20 - 1800 K, [61], CS, SHC, XS
Pt	Platinum	93	Pt	20 - 2000 K, [62], CS, SHC, XS
Rb	Rubidium	94	Rb	20 - 300 K, [63], CS, SHC, XS
Sc	Scandium	96	Sc	20 - 1800 K, [64], CS, SHC, XS
SiC- α	Alpha Silicon Carbide	98	C(SiC- α), Si(SiC- α)	1973 - 3100 K, [13], CS, DIFF
SiC- β	Beta Silicon Carbide	99	C(SiC- β), Si(SiC- β)	20 - 1900 K [13], CS, DIFF

* CS = Crystal structure

* SHC = Specific heat capacity

* XS = Total cross section measurement

* DIFF = Diffraction data

Table 6
List of tsl-ENDF evaluations in the NJOY+NCrystal library (continued)

Material	Name	Material Number	Components	Temperature range, VDOS reference, Validation
SiLu2O5	Silicon Lutetium Oxide	100	O(SiLu2O5), Si(SiLu2O5), Lu(SiLu2O5)	20 - 2400 K, [13], CS, SHC
SiO2- α	Alpha Quartz	101	O(SiO2- α), Si(SiO2- α)	20 - 800 K, [13], CS, SHC, XS
SiO2- β	Beta Quartz	102	O(SiO2- β), Si(SiO2- β)	846.15 - 1900 K, [13], CS, SHC
SiY2O5	Silicon Yttrium Oxide	103	O(SiY2O5), Si(SiY2O5), Y(SiY2O5)	20 - 2300 K, [13], CS, SHC
Si	Silicon	104	Si	20 - 1600 K, [65], CS, SHC, XS
Sn	Tin	107	Sn	20 - 500 K, [66], CS, SHC, XS
SrF2	Strontium Fluoride	108	F(SrF2), Sr(SrF2)	20 - 1400 K, [13], CS, SHC
SrH2	Strontium Hydride	109	H(SrH2), Sr(SrH2)	20 - 1300 K, [13], CS, SHC
Sr	Strontium	111	Sr	20 - 1000 K, [67], CS, SHC
Th3N4	Thorium Nitride	112	N(Th3N4), Th(Th3N4)	20 - 3000 K, [13], CS, SHC
ThO2	Thorium Dioxide	113	O(ThO2), Th(ThO2)	20 - 3500 K, [13], CS, SHC
ThSiO4	Huttonite	114	O(ThSiO4), Si(ThSiO4), Th(ThSiO4)	20 - 2000 K, [13], CS, SHC
TiO2-anatase	Anatase	115	O(TiO2-anatase), Ti(TiO2-anatase)	20 - 2000 K, [13], CS, SHC
TiO2-rutile	Rutile	116	O(TiO2-rutile), Ti(TiO2-rutile)	873 - 2000 K, [13], CS, SHC
Ti	Titanium	117	Ti	20 - 1800 K, [68], CS, SHC, XS
TlBr	Thalium Bromide	118	Br(TlBr), Tl(TlBr)	20 - 700 K, [13], CS, SHC
Tm2O3	Thulium Oxide	119	O(Tm2O3), Tm(Tm2O3)	20 - 2400 K, [13], CS, SHC
UF6	Uranium Hexafluoride	120	F(UF6), U(UF6)	20 - 320 K, [13], CS, SHC
V	Vanadium	122	V	20 - 2000 K, [69], CS, SHC, XS
W	Tungsten	123	W	20 - 3500 K, [70], CS, SHC, XS

* CS = Crystal structure

* SHC = Specific heat capacity

* XS = Total cross section measurement

Table 7
List of tsl-ENDF evaluations in the NJOY+NCrystal library (continued)

Material	Name	Material Number	Components	Temperature range, VDOS reference, Validation
Y2O3	Yttrium Oxide	124	O(Y2O3), Y(Y2O3)	20 - 2500 K, [71], CS, SHC
Y3Al5O12	Yttrium Aluminium Garnet	125	O(Y3Al5O12), Al(Y3Al5O12), Y(Y3Al5O12)	20 - 2900 K, [13], CS, SHC
YAlO3	Yttrium Orthoaluminate	126	O(YAlO3), Al(YAlO3), Y(YAlO3)	20 - 2000 K, [13], CS, SHC
Y	Yttrium	127	Y	20 - 1600 K, [72], CS, SHC, XS
ZnF2	Zinc Flouride	128	F(ZnF2), Zn(ZnF2)	20 - 1000 K, [13], CS, SHC
ZnO	Zinc Oxide	129	O(ZnO), Zn(ZnO)	20 - 2200 K, [13], CS, SHC
ZnS-sphalerite	Zinc Sulfide	130	S(ZnS-sphalerite), Zn(ZnS-sphalerite)	20 - 1300 K, [13], CS, SHC
Zn	Zinc	131	Zn	20 - 600 K, [73], CS, SHC, XS
ZrF4- β	Beta Zirconium Tetrafluoride	132	F(ZrF4- β), Zr(ZrF4- β)	773 - 1150 K, [13], CS, SHC
ZrO2-tet	Tetragonal Zirconium Dioxide	133	O(ZrO2-tet), Zr(ZrO2-tet)	1443.15 - 2600 K, [13], CS, SHC
ZrO2	Zirconium Dioxide	134	O(ZrO2), Zr(ZrO2)	20 - 1400 K, [13], CS, SHC
ZrSiO4	Zirconium Orthosilicate	135	O(ZrSiO4), Si(ZrSiO4), Zr(ZrSiO4)	20 - 1800 K, [13], CS, SHC
Zr	Zirconium	136	Zr	20 - 2000 K, [70], CS, SHC, XS

* CS = Crystal structure

* SHC = Specific heat capacity

* XS = Total cross section measurement

References

- [1] HighNESS Project. HighNESS project description. <https://highnessproject.eu/mission-and-objectives/>, 2020. [Online].
- [2] V. Santoro, K. H. Andersen, D. D. DiJulio, E. B. Klinkby, T. M. Miller, D. Milstead, G. Muhrer, M. Strobl, A. Takibayev, L. Zanini, and et al. Development of high intensity neutron source at the European Spallation Source. *Journal of Neutron Research*, (Preprint):1–11, 2020.
- [3] J. Goorley, M. James, and et al. Initial MCNP6 Release Overview. Technical Report LA-UR-13-22934, Los Alamos National Laboratory, 2013.
- [4] P. K. Romano, N. E. Horelik, B. R. Herman, A. G. Nelson, B. Forget, and K. Smith. OpenMC: A state-of-the-art Monte Carlo code for research and development. *Annals of Nuclear Energy*, 82:90–97, 2015. ISSN 0306-4549. doi: <https://doi.org/10.1016/j.anucene.2014.07.048>. URL <https://www.sciencedirect.com/science/article/pii/S030645491400379X>. Joint International Conference on Supercomputing in Nuclear Applications and Monte Carlo 2013, SNA + MC 2013. Pluri- and Trans-disciplinarity, Towards New Modeling and Numerical Simulation Paradigms.
- [5] T. Sato, Y. Iwamoto, S. Hashimoto, T. Ogawa, T. Furuta, S. Abe, T. Kai, P. Tsai, N. Matsuda, H. Iwase, N. Shigyo, L. Sihver, and K. Niita. Features of Particle and Heavy Ion Transport code System (PHITS) version 3.02. *Journal of Nuclear Science and Technology*, 55(6):684–690, 2018. doi: 10.1080/00223131.2017.1419890. URL <https://doi.org/10.1080/00223131.2017.1419890>.
- [6] A. Trkov and D. A. Brown. ENDF-6 Formats Manual: Data Formats and Procedures for the Evaluated Nuclear Data Files. 1 2018. doi: 10.2172/1425114. URL <https://www.osti.gov/biblio/1425114>.
- [7] M. Zerkle. TSL mixed elastic scattering format. <https://indico.bnl.gov/event/7233/contributions/43822/>, 2020.
- [8] R.E. MacFarlane and A.C. Kahler. Methods for Processing ENDF/B-VII with NJOY. *Nuclear Data Sheets*, 111(12):2739–2890, 2010. ISSN 0090-3752. doi: <https://doi.org/10.1016/j.nds.2010.11.001>. URL <http://www.sciencedirect.com/science/article/pii/S0090375210001006>. Nuclear Reaction Data.
- [9] X.-X. Cai and T. Kittelmann. NCrystal: A library for thermal neutron transport. *Computer Physics Communications*, 246:106851, 2020. ISSN 0010-4655. doi: <https://doi.org/10.1016/j.cpc.2019.07.015>. URL <https://www.sciencedirect.com/science/article/pii/S0010465519302280>.
- [10] X.-X. Cai, T. Kittelmann, E. Klinkby, and J.I. Márquez Damián. Rejection-based sampling of inelastic neutron scattering. *Journal of Computational Physics*, 380:400–407, 2019. ISSN 0021-9991. doi: <https://doi.org/10.1016/j.jcp.2018.11.043>. URL <https://www.sciencedirect.com/science/article/pii/S0021999118307885>.
- [11] J.L. Conlin. ACE—A Compact ENDF—Format Specification. <https://github.com/NuclearData/ACEFormat>, 2020.
- [12] HighNESS WP2. NJOY+NCrystal OpenMC Github repository. https://github.com/highness-eu/openmc/tree/njoy_ncrystal, 2021. [Online].
- [13] A. Togo. Phonon database at Kyoto University. <http://phonondb.mtl.kyoto-u.ac.jp/>, 2015. [Online].
- [14] A. Jain, S. P. Ong, G. Hautier, W. Chen, W. D. Richards, S. Dacek, S. Cholia, D. Gunter, D. Skinner, G. Ceder, and K. A. Persson. Commentary: The Materials Project: A materials genome approach to accelerating materials innovation. *APL Materials*, 1(1):011002, 2013. doi: 10.1063/

- 1.4812323. URL <https://doi.org/10.1063/1.4812323>.
- [15] S. P. Ong, W. D. Richards, A. Jain, G. Hautier, M. Kocher, S. Cholia, D. Gunter, V. L. Chevrier, K. A. Persson, and G. Ceder. Python Materials Genomics (pymatgen): A robust, open-source python library for materials analysis. *Computational Materials Science*, 68:314–319, 2013. ISSN 0927-0256. doi: <https://doi.org/10.1016/j.commatsci.2012.10.028>. URL <https://www.sciencedirect.com/science/article/pii/S0927025612006295>.
- [16] S. P. Ong, S. Cholia, A. Jain, M. Brafman, D. Gunter, G. Ceder, and K. A. Persson. The Materials Application Programming Interface (API): A simple, flexible and efficient API for materials data based on REpresentational State Transfer (REST) principles. *Computational Materials Science*, 97:209–215, 2015. ISSN 0927-0256. doi: <https://doi.org/10.1016/j.commatsci.2014.10.037>. URL <https://www.sciencedirect.com/science/article/pii/S0927025614007113>.
- [17] A. Togo and I. Tanaka. First principles phonon calculations in materials science. *Scr. Mater.*, 108:1–5, Nov 2015.
- [18] Y. Q. Cheng, L. L. Daemen, A. I. Kolesnikov, and A. J. Ramirez-Cuesta. Simulation of Inelastic Neutron Scattering Spectra Using OCLIMAX. *Journal of Chemical Theory and Computation*, 15(3):1974–1982, 2019.
- [19] R. E. Mayer, F. Kropff, and J. R. Granada. Total neutron cross section of tin in the energy range from 6.3e-4 eV to 15.8 eV. *Atomkernenerg./Kerntech.*, 39(1), 1981.
- [20] IAEA-NDS. Exfor dataset 30592002, . URL <http://www-nds.iaea.org/exfor/>.
- [21] N. Otuka, E. Dupont, V. Semkova, B. Pritychenko, A. I. Blokhin, M. Aikawa, S. Babykina, M. Bossant, G. Chen, S. Dunaeva, and et al. Towards a more complete and accurate experimental nuclear reaction data library (EXFOR): international collaboration between nuclear reaction data centres (NRDC). *Nuclear Data Sheets*, 120:272–276, 2014.
- [22] IAEA-NDS. Exfor dataset 40294002, . URL <http://www-nds.iaea.org/exfor/>.
- [23] IAEA-NDS. Exfor dataset 11663002, . URL <http://www-nds.iaea.org/exfor/>.
- [24] R. G. Allen, T.E Stephenson, C. P. Stanford, and S. Bernstein. Slow neutron cross sections of gold, silver, indium, nickel, and nickel oxide. *Physical Review*, 96(5):1297, 1954.
- [25] IAEA-NDS. Exfor dataset 11762002, . URL <http://www-nds.iaea.org/exfor/>.
- [26] D. J. Hughes and R. B. Schwartz. *Neutron cross sections - Report BNL 325*. Brookhaven National Laboratory, 1958.
- [27] IAEA-NDS. Exfor dataset 11355002, . URL <http://www-nds.iaea.org/exfor/>.
- [28] J. R. Granada, J. I. Márquez Damián, J. Dawidowski, J. I. Robledo, C. Helman, G. Romanelli, and G. Škoro. Development of neutron scattering kernels for cold neutron reflector materials, 2021.
- [29] S. Baroni, S. De Gironcoli, A. Dal Corso, and P. Giannozzi. Phonons and related crystal properties from density-functional perturbation theory. *Reviews of Modern Physics*, 73(2):515–562, jul 2001. ISSN 00346861. doi: 10.1103/RevModPhys.73.515. URL <http://link.aps.org/doi/10.1103/RevModPhys.73.515>.
- [30] J. P. Perdew, K. Burke, and M. Ernzerhof. Generalized Gradient Approximation Made Simple. *Phys. Rev. Lett*, 77:3865, 1996.
- [31] D. Vanderbilt. Soft self-consistent pseudopotentials in a generalized eigenvalue formalism. *Phys. Rev. B*, 41:7892–7895, Apr 1990. doi:

- 10.1103/PhysRevB.41.7892. URL <https://link.aps.org/doi/10.1103/PhysRevB.41.7892>.
- [32] A. Dal Corso. Pseudopotentials periodic table: From H to Pu. *Computational Materials Science*, 95:337–350, 2014. ISSN 0927-0256. doi: <https://doi.org/10.1016/j.commatsci.2014.07.043>. URL <https://www.sciencedirect.com/science/article/pii/S0927025614005187>.
- [33] P. Giannozzi, S. Baroni, N. Bonini, M. Calandra, R. Car, C. Cavazzoni, D. Ceresoli, G. L. Chiarotti, M. Cococcioni, I. Dabo, A. Dal Corso, S. de Gironcoli, S. Fabris, G. Fratesi, R. Gebauer, U. Gerstmann, C. Gougoussis, A. Kokalj, M. Lazzeri, L. Martin-Samos, N. Marzari, F. Mauri, R. Mazzarello, S. Paolini, A. Pasquarello, L. Paulatto, C. Sbraccia, S. Scandolo, G. Sclauzero, A. P. Seitsonen, A. Smogunov, P. Umari, and R. M. Wentzcovitch. QUANTUM ESPRESSO: a modular and open-source software project for quantum simulations of materials. *J. Phys.: Condens. Matter*, 21(39):395502, 2009. URL <http://stacks.iop.org/0953-8984/21/i=39/a=395502>.
- [34] H.J. Monkhorst and J. D. Pack. Special points for Brillouin-zone integrations. *Phys. Rev. B*, 13:5188, 1976.
- [35] F. H. Ellinger, C. E. Holley, B. B. McInteer, D. Pavone, R. M. Potter, E. Staritzky, and W. H. Zachariasen. The Preparation and Some Properties of Magnesium Hydride. *Journal of the American Chemical Society*, 77(9):2647–2648, May 1955. ISSN 0002-7863. doi: 10.1021/ja01614a094. URL <https://doi.org/10.1021/ja01614a094>.
- [36] N. Ohba, K. Miwa, T. Noritake, and A. Fukumoto. First-principles study on thermal vibration effects of MgH₂. *Phys. Rev. B*, 70:035102, 2004.
- [37] H.G. Schimmel, M.R. Johnson, G.J. Kearley, A.J. Ramirez-Cuesta, J. Huot, and F.M. Mulder. The vibrational spectrum of magnesium hydride from inelastic neutron scattering and density functional theory. *Mat. Sci. and Eng. B*, 108:38, 2004.
- [38] V. F. Sears. Neutron scattering lengths and cross sections. *Neutron News*, 3(3):26–37, 1992. doi: 10.1080/10448639208218770. URL <https://doi.org/10.1080/10448639208218770>.
- [39] A.I. Kolesnikov, V.E. Antonov, V.S. Efimchenko, G. Granroth, S.N. Klyamkin, A.V. Levchenko, M.K. Sakharov, and Y. Ren. Neutron spectroscopy of magnesium dihydride. *Journal of Alloys and Compounds*, 509:S599–S603, 2011. ISSN 0925-8388. doi: <https://doi.org/10.1016/j.jallcom.2010.10.156>. URL <https://www.sciencedirect.com/science/article/pii/S0925838810026861>. Proceedings of the 12th International Symposium on Metal-Hydrogen Systems, Fundamentals and Applications (MH2010).
- [40] W. Cai, H. Li, X. Zhou, L. Xia, and S. Peng. Temperature-dependent lattice vibration of magnesium hydride. *The Journal of Physical Chemistry C*, 122(49):27963–27972, 2018. doi: 10.1021/acs.jpcc.8b10294. URL <https://doi.org/10.1021/acs.jpcc.8b10294>.
- [41] G. L. W. Hart, L. J. Nelson, R. R. Vanfleet, B. J. Campbell, M. H. F. Sluiter, J. H. Neethling, E. J. Olivier, S. Allies, C. I. Lang, B. Meredig, and C. Wolverton. Revisiting the revised Ag-Pt phase diagram. *Acta Materialia*, 124:325–332, 2017. ISSN 1359-6454. doi: <https://doi.org/10.1016/j.actamat.2016.10.053>. URL <https://www.sciencedirect.com/science/article/pii/S1359645416308205>.
- [42] Z. Łodziana and K. Parliński. Dynamical stability of the α and θ phases of alumina. *Phys. Rev. B*, 67:174106, May 2003. doi: 10.1103/PhysRevB.67.174106. URL <https://link.aps.org/doi/10.1103/PhysRevB.67.174106>.
- [43] A. Togo and I. Tanaka. First principles phonon calculations in materials science. *Scripta Materialia*, 108:1–5, 2015. ISSN 1359-6462. doi: <https://doi.org/10.1016/j.scriptamat.2015.07.021>. URL <https://www.sciencedirect.com/science/article/pii/S1359646215000000>.

S1359646215003127.

- [44] H. R. Schober and P. H. Dederichs. Phonon States of Elements. Electron States and Fermi Surfaces of Alloys · Au: Datasheet from Landolt-Börnstein - Group III Condensed Matter · Volume 13A: “Phonon States of Elements. Electron States and Fermi Surfaces of Alloys” in SpringerMaterials (https://doi.org/10.1007/10201666_5), . URL https://materials.springer.com/lb/docs/sm_lbs_978-3-540-38957-6_5. Copyright 1981 Springer-Verlag Berlin Heidelberg.
- [45] B. A. Oli. Microscopic theory of the phonon frequencies in BCC barium. URL https://inis.iaea.org/search/search.aspx?orig_q=RN:20020262.
- [46] J. Keinert, S. Käfer, and M. Mattes. Evaluation of coherent and incoherent thermal neutron scattering cross-sections for polycrystalline bismuth /Evaluierung von Wirkungsquerschnitten für kohärente und inkohärente Streuung thermischer Neutronen in polykristallinem Wismut. *Kerntechnik*, 57(4):233–236, 1992. doi: doi:10.1515/kern-1992-570412. URL <https://doi.org/10.1515/kern-1992-570412>.
- [47] J. Xie, S. P. Chen, J. S. Tse, S. de Gironcoli, and S. Baroni. High-pressure thermal expansion, bulk modulus, and phonon structure of diamond. *Phys. Rev. B*, 60:9444–9449, Oct 1999. doi: 10.1103/PhysRevB.60.9444. URL <https://link.aps.org/doi/10.1103/PhysRevB.60.9444>.
- [48] C. Stassis, J. Zaretsky, D. K. Misemer, H. L. Skriver, B. N. Harmon, and R. M. Nicklow. Lattice dynamics of fcc Ca. *Phys. Rev. B*, 27:3303–3307, Mar 1983. doi: 10.1103/PhysRevB.27.3303. URL <https://link.aps.org/doi/10.1103/PhysRevB.27.3303>.
- [49] H. R. Schober and P. H. Dederichs. Phonon States of Elements. Electron States and Fermi Surfaces of Alloys · Cr: Datasheet from Landolt-Börnstein - Group III Condensed Matter · Volume 13A: “Phonon States of Elements. Electron States and Fermi Surfaces of Alloys” in SpringerMaterials (https://doi.org/10.1007/10201666_13), . URL https://materials.springer.com/lb/docs/sm_lbs_978-3-540-38957-6_13. Copyright 1981 Springer-Verlag Berlin Heidelberg.
- [50] R. M. Nicklow, G. Gilat, H. G. Smith, L. J. Raubenheimer, and M. K. Wilkinson. Phonon Frequencies in Copper at 49 and 298°K. *Phys. Rev.*, 164:922–928, Dec 1967. doi: 10.1103/PhysRev.164.922. URL <https://link.aps.org/doi/10.1103/PhysRev.164.922>.
- [51] V. J. Minkiewicz, G. Shirane, and R. Nathans. Phonon Dispersion Relation for Iron. *Phys. Rev.*, 162:528–531, Oct 1967. doi: 10.1103/PhysRev.162.528. URL <https://link.aps.org/doi/10.1103/PhysRev.162.528>.
- [52] J. Zaretsky and C. Stassis. Lattice dynamics of γ -Fe. *Phys. Rev. B*, 35:4500–4502, Mar 1987. doi: 10.1103/PhysRevB.35.4500. URL <https://link.aps.org/doi/10.1103/PhysRevB.35.4500>.
- [53] G. Nelin and G. Nilsson. Phonon Density of States in Germanium at 80 K Measured by Neutron Spectrometry. *Phys. Rev. B*, 5:3151–3160, Apr 1972. doi: 10.1103/PhysRevB.5.3151. URL <https://link.aps.org/doi/10.1103/PhysRevB.5.3151>.
- [54] H. R. Schober and P. H. Dederichs. Phonon States of Elements. Electron States and Fermi Surfaces of Alloys · K: Datasheet from Landolt-Börnstein - Group III Condensed Matter · Volume 13A: “Phonon States of Elements. Electron States and Fermi Surfaces of Alloys” in SpringerMaterials (https://doi.org/10.1007/10201666_24), . URL https://materials.springer.com/lb/docs/sm_lbs_978-3-540-38957-6_24. Copyright 1981 Springer-Verlag Berlin Heidelberg.
- [55] H. R. Schober and P. H. Dederichs. Phonon States of Elements. Electron States and Fermi Surfaces of Alloys · Mg: Datasheet from

- Landolt-Börnstein - Group III Condensed Matter · Volume 13A: “Phonon States of Elements. Electron States and Fermi Surfaces of Alloys” in SpringerMaterials (https://doi.org/10.1007/10201666_26), . URL https://materials.springer.com/lb/docs/sm_lbs_978-3-540-38957-6_26. Copyright 1981 Springer-Verlag Berlin Heidelberg.
- [56] H. R. Schober and P. H. Dederichs. Phonon States of Elements. Electron States and Fermi Surfaces of Alloys · Mo: Datasheet from Landolt-Börnstein - Group III Condensed Matter · Volume 13A: “Phonon States of Elements. Electron States and Fermi Surfaces of Alloys” in SpringerMaterials (https://doi.org/10.1007/10201666_27), . URL https://materials.springer.com/lb/docs/sm_lbs_978-3-540-38957-6_27. Copyright 1981 Springer-Verlag Berlin Heidelberg.
- [57] H. R. Schober and P. H. Dederichs. Phonon States of Elements. Electron States and Fermi Surfaces of Alloys · Na: Datasheet from Landolt-Börnstein - Group III Condensed Matter · Volume 13A: “Phonon States of Elements. Electron States and Fermi Surfaces of Alloys” in SpringerMaterials (https://doi.org/10.1007/10201666_28), . URL https://materials.springer.com/lb/docs/sm_lbs_978-3-540-38957-6_28. Copyright 1981 Springer-Verlag Berlin Heidelberg.
- [58] H. R. Schober and P. H. Dederichs. Phonon States of Elements. Electron States and Fermi Surfaces of Alloys · Nb: Datasheet from Landolt-Börnstein - Group III Condensed Matter · Volume 13A: “Phonon States of Elements. Electron States and Fermi Surfaces of Alloys” in SpringerMaterials (https://doi.org/10.1007/10201666_29), . URL https://materials.springer.com/lb/docs/sm_lbs_978-3-540-38957-6_29. Copyright 1981 Springer-Verlag Berlin Heidelberg.
- [59] M. Kresch, O. Delaire, R. Stevens, J. Y. Y. Lin, and B. Fultz. Neutron scattering measurements of phonons in nickel at elevated temperatures. *Phys. Rev. B*, 75:104301, Mar 2007. doi: 10.1103/PhysRevB.75.104301. URL <https://link.aps.org/doi/10.1103/PhysRevB.75.104301>.
- [60] G. Gilat. Phonon density states in lead. *Solid State Communications*, 3(5):101–103, 1965. ISSN 0038-1098. doi: [https://doi.org/10.1016/0038-1098\(65\)90232-2](https://doi.org/10.1016/0038-1098(65)90232-2). URL <https://www.sciencedirect.com/science/article/pii/0038109865902322>.
- [61] H. R. Schober and P. H. Dederichs. Phonon States of Elements. Electron States and Fermi Surfaces of Alloys · Pd: Datasheet from Landolt-Börnstein - Group III Condensed Matter · Volume 13A: “Phonon States of Elements. Electron States and Fermi Surfaces of Alloys” in SpringerMaterials (https://doi.org/10.1007/10201666_32), . URL https://materials.springer.com/lb/docs/sm_lbs_978-3-540-38957-6_32. Copyright 1981 Springer-Verlag Berlin Heidelberg.
- [62] H. R. Schober and P. H. Dederichs. Phonon States of Elements. Electron States and Fermi Surfaces of Alloys · Pt: Datasheet from Landolt-Börnstein - Group III Condensed Matter · Volume 13A: “Phonon States of Elements. Electron States and Fermi Surfaces of Alloys” in SpringerMaterials (https://doi.org/10.1007/10201666_33), . URL https://materials.springer.com/lb/docs/sm_lbs_978-3-540-38957-6_33. Copyright 1981 Springer-Verlag Berlin Heidelberg.
- [63] H. R. Schober and P. H. Dederichs. Phonon States of Elements. Electron States and Fermi Surfaces of Alloys · Rb: Datasheet from Landolt-Börnstein - Group III Condensed Matter · Volume 13A: “Phonon States of Elements. Electron States and Fermi Surfaces of Alloys” in SpringerMaterials (https://doi.org/10.1007/10201666_34), . URL https://materials.springer.com/lb/docs/sm_lbs_978-3-540-38957-6_34. Copyright 1981 Springer-Verlag Berlin Heidelberg.

- [64] H. R. Schober and P. H. Dederichs. Phonon States of Elements. Electron States and Fermi Surfaces of Alloys · Sc: Datasheet from Landolt-Börnstein - Group III Condensed Matter · Volume 13A: “Phonon States of Elements. Electron States and Fermi Surfaces of Alloys” in SpringerMaterials (https://doi.org/10.1007/10201666_38), . URL https://materials.springer.com/lb/docs/sm_lbs_978-3-540-38957-6_38. Copyright 1981 Springer-Verlag Berlin Heidelberg.
- [65] Z. Liu, Y. Wang, and S. Shang. Thermal Expansion Anomaly Regulated by Entropy. *Scientific Reports*, 4(1):7043, Nov 2014. ISSN 2045-2322. doi: 10.1038/srep07043. URL <https://doi.org/10.1038/srep07043>.
- [66] A. Barla, R. Ruffer, A. I. Chumakov, J. Metge, J. Plessel, and M. M. Abd-Elmeguid. Direct determination of the phonon density of states in β -Sn. *Phys. Rev. B*, 61:R14881–R14884, Jun 2000. doi: 10.1103/PhysRevB.61.R14881. URL <https://link.aps.org/doi/10.1103/PhysRevB.61.R14881>.
- [67] U. Buchenau, M. Heiroth, H. R. Schober, J. Evers, and G. Oehlinger. Lattice dynamics of strontium and barium. *Phys. Rev. B*, 30:3502–3505, Sep 1984. doi: 10.1103/PhysRevB.30.3502. URL <https://link.aps.org/doi/10.1103/PhysRevB.30.3502>.
- [68] C. Stassis, D. Arch, B. N. Harmon, and N. Wakabayashi. Lattice dynamics of hcp Ti. *Phys. Rev. B*, 19:181–188, Jan 1979. doi: 10.1103/PhysRevB.19.181. URL <https://link.aps.org/doi/10.1103/PhysRevB.19.181>.
- [69] J. A. Muñoz, M. S. Lucas, O. Delaire, M. L. Winterrose, L. Mauger, Chen W. Li, A. O. Sheets, M. B. Stone, D. L. Abernathy, Yuming Xiao, Paul Chow, and B. Fultz. Positive Vibrational Entropy of Chemical Ordering in FeV. *Phys. Rev. Lett.*, 107:115501, Sep 2011. doi: 10.1103/PhysRevLett.107.115501. URL <https://link.aps.org/doi/10.1103/PhysRevLett.107.115501>.
- [70] J. Crocombette, P. Notargiacomo, and M. Marinica. Effect of the variation of the electronic density of states of zirconium and tungsten on their respective thermal conductivity evolution with temperature. *Journal of Physics: Condensed Matter*, 27(16):165501, mar 2015. doi: 10.1088/0953-8984/27/16/165501. URL <https://doi.org/10.1088/0953-8984/27/16/165501>.
- [71] P. P. Bose, M. K. Gupta, R. Mittal, S. Rols, S. N. Achary, A. K. Tyagi, and S. L. Chaplot. Phase transitions and thermodynamic properties of yttria, Y_2O_3 : Inelastic neutron scattering shell model and first-principles calculations. *Phys. Rev. B*, 84:094301, Sep 2011. doi: 10.1103/PhysRevB.84.094301. URL <https://link.aps.org/doi/10.1103/PhysRevB.84.094301>.
- [72] H. R. Schober and P. H. Dederichs. Phonon States of Elements. Electron States and Fermi Surfaces of Alloys · Y: Datasheet from Landolt-Börnstein - Group III Condensed Matter · Volume 13A: “Phonon States of Elements. Electron States and Fermi Surfaces of Alloys” in SpringerMaterials (https://doi.org/10.1007/10201666_50), . URL https://materials.springer.com/lb/docs/sm_lbs_978-3-540-38957-6_50. Copyright 1981 Springer-Verlag Berlin Heidelberg.
- [73] H. R. Schober and P. H. Dederichs. Phonon States of Elements. Electron States and Fermi Surfaces of Alloys · Zn: Datasheet from Landolt-Börnstein - Group III Condensed Matter · Volume 13A: “Phonon States of Elements. Electron States and Fermi Surfaces of Alloys” in SpringerMaterials (https://doi.org/10.1007/10201666_51), . URL https://materials.springer.com/lb/docs/sm_lbs_978-3-540-38957-6_51. Copyright 1981 Springer-Verlag Berlin Heidelberg.